PERGAMON

International Journal of Solids and Structures 37 (2000) 7093–7104

INTERNATIONAL JOURNAL OF SOLIDS and STRUCTURES

www.elsevier.com/locate/ijsolstr

Crack analysis in ductile cylindrical shells using Gurson's model

H. Baaser, D. Gross *

Institute of Mechanics, Darmstadt University of Technology, Hochschulstrasse 1, D–64289 Darmstadt, Germany

Received 10 November 1999

Abstract

Damage evolution in cracked cylindrical shells subjected to uniform pressure is numerically simulated using finite 3D-continuum elements. The ductile material behaviour of mild steel is described in terms of the Gurson damage model. To represent the stress and damage distribution across the wall thickness, three element layers normal to the shell surface were used. The description of finite plasticity is based on the multiplicative split of the deformation gradient. The numerical method is applied to investigate damage evolution, crack initiation and growth in a tube under pressure containing an axial and a circumferential through-crack. © 2000 Elsevier Science Ltd. All rights reserved.

Keywords: Shells; Damage; Finite plasticity; 3D solid element

1. Introduction

Shells or shell-like structures are common elements in mechanical and civil engineering. Therefore, a significant research interest has been devoted to these types of structures for many years. However, while the different models and the analytical and numerical methods can be successfully applied to many classes of problems, there is still room for improvements, especially in view of a more detailed local analysis and more sophisticated constitutive laws.

As a lot of engineering problems are endowed with geometrical or material nonlinearities, the finite element method has become a useful tool for treating shell-like structures. Although the development of special shell elements is extremely advanced (see e.g. Wriggers et al., 1996), their application is in most cases restricted to specific geometries. As an example, due to complicated shapes of certain modern engineering structures, common simplifications in shell theory (e.g. the thin shell hypothesis) become less adequate. An attractive idea to overcome these simplifications is to model shells not by special shell elements but to consider such structures as general 3D-continua which are numerically modelled by 3D-elements. Such a concept was applied and compared with shell formulations in a few recent investigations, see Wriggers et al. (1996) and Roehl and Ramm (1996). It offers (at least in principle) the opportunity for a more detailed analysis of local 3D-phenomena, which was not done by the mentioned works.

* Corresponding author. Tel.: +49-6151-162973; fax: +49-6151-163018.
E-mail address: gross@mechanik.tu-darmstadt.de (D. Gross).

PII: S0020-7683(99)00329-7

If a shell contains a crack or another type of stress concentrator, generally local 3D-stress fields occur which cannot be modelled by usual shell elements. Therefore, it is desirable to develop simple but still numerically stable 3D-continuum element formulations, which are able to model such problems with sufficient accuracy. Unfortunately, the computer memory requirement rises considerably when using 3D-elements, limiting even today their wider application. However, this aspect will become less important when keeping in mind the rapid development of computer technology.

Damage as a pre-failure material state and in its final stage as failure indicator is of high interest in modern fracture mechanics. It is well known that especially 3D-effects accompanied with crack initiation and crack growth in ductile materials can be described properly by applying appropriate continuum damage models. Examples of such studies, based on the Gurson damage model and concentrated on the damage and failure behaviour of test specimen used in ductile fracture mechanics, can be found in Klingbeil et al. (1993) and Klingbeil and Zadeh (1995). The results indicate that the detailed fracture process generally can be better described by damage parameters than by conventional fracture quantities like for e.g. the J-integral. Though ductile damage descriptions proved to be very useful in fracture mechanics, direct applications to structures are very rare. The reasons for this may be found on the one hand in the numerical expense and the numerical problems (e.g. mesh-dependent results) accompanied with the use of strain softening material models and on the other hand in the fact that necessary material parameters are often not available and difficult to measure.

The aim of this study is to show that ductile damage models may be applied to investigate the damage and fracture process in shell-like structures using finite 3D-continuum elements. The elastic–plastic damaging material behaviour is described by Gurson's model (1977) in the version of Tvergaard (1989). This model interprets the occurrence, growth and coalescence of microvoids as *damage* which is characterized by the scalar field f – the void volume fraction. In order to introduce as little restrictions as possible, finite deformations are taken into account. There are reasonable continuum-element formulations available in the literature which are able to describe von Mises-plasticity or hyperelastic material models based on finite deformations, see Wriggers et al. (1996) and the cited literature herein. The formulation, numerical treatment and handling of this kind of 3D-modeling is well understood. Here, we generalize these formulations by introducing the Gurson model and apply it to simple 8-node displacement elements used for the spatial discretization of the structure. The emphasis of this study lies on the realization and application of the numerical scheme. Not considered are critical aspects of the damage model and questions regarding the determination of material parameters.

As examples, damage evolution, crack initiation and crack growth in a CT test specimen and in cylindrical shells containing a through-crack subjected to increasing load are analysed. As a similar problem was treated in Baaser and Gross (1998a) by a shell formulation, the present investigation can be regarded as a continuation and generalization of that work to model through-cracked shell structures. To the knowledge of the authors such an investigation, using continuum elements instead of more complicated shell elements in conjunction with the Gurson damage model, is not available in the literature.

2. Damage model and finite plasticity

2.1. Damage model

Constitutive basis of this study is the damage model proposed by Gurson (1977) and modified in Tvergaard (1989). It may be interpreted as an extension of conventional v. Mises plasticity, taking into account the experimental observation that ductile degradation processes consist of the nucleation, the growth and the coalescence of microvoids. The volume fraction f of the voids is chosen as damage pa-

rameter. Since the model is extensively described and discussed in a series of papers, see Tvergaard (1989), only a short outline is presented here.

The Gurson yield function which takes into account ductile damage processes may be written as

$$\Phi = \left(\frac{\sigma_e}{\sigma_M}\right)^2 + 2q_1 f^* \cosh\left(\frac{\sigma_{kk}}{2\sigma_M}\right) - \left[1 + (q_1 f^*)^2\right] = 0, \tag{1}$$

where $\sigma_e = (\frac{3}{2} s_{ij} s_{ij})^{1/2}$ is the equivalent macroscopic stress, $s_{ij} = \sigma_{ij} - \frac{1}{3}\sigma_{kk}\delta_{ij}$, the stress deviator and σ_{ij}, the Cauchy stress tensor. By σ_M the current (microscopic) yield stress of the matrix material (without voids) is represented, f^* is the effective void volume fraction (Tvergaard, 1989) and q_1 denotes a material parameter which is chosen here (as in other investigations) as $q_1 = 1.5$. It is obvious that Φ depends directly on the damage variable f. The range of the possible elastic states described by $\Phi < 0$ shrinks with increasing f and loss of stress carrying capacity occurs. In space discretizing methods this softening leads to mesh dependent results, if no additional regularization is introduced.

The macroscopic plastic strain rate $\dot{\boldsymbol{\epsilon}}^{pl}$ is determined by the classical flow rule

$$\dot{\boldsymbol{\epsilon}}^{pl} = \dot{\lambda}\frac{\partial \Phi}{\partial \boldsymbol{\sigma}}, \tag{2}$$

while the damage evolution $\dot{f} = \dot{f}_{grw} + \dot{f}_{nucl}$ is assumed to consist of the two parts

$$\dot{f}_{grw} = (1-f)\dot{\epsilon}^{pl}_{kk}, \qquad \dot{f}_{nucl} = \frac{f_N}{s_N\sqrt{2\pi}} \exp\left[-\frac{1}{2}\left(\frac{\varepsilon^{pl}_M - \varepsilon_N}{s_N}\right)^2\right]\dot{\varepsilon}^{pl}_M. \tag{3}$$

Here, $\dot{f}_{grw}$ and $\dot{f}_{nucl}$ describe the growth of the existing voids and the strain controlled nucleation of new voids, respectively, and f_N, ε_N and s_N are material parameters. Further, ε^{pl}_M represents the equivalent plastic strain of the matrix material, which is determined by the assumption of equivalence of the plastic work increments on the microscopic and macroscopic level:

$$(1-f)\sigma_M \dot{\varepsilon}^{pl}_M = \boldsymbol{\sigma}\,\dot{\boldsymbol{\epsilon}}^{pl}. \tag{4}$$

Finally, to get a complete set of constitutive equations, the behaviour of the matrix material is approximated by the power law

$$\sigma_M = \sigma_0\left(\frac{\varepsilon^{pl}_M}{\varepsilon_0} + 1\right)^{1/N}, \tag{5}$$

where N is the hardening exponent, $\sigma_0 = E\,\varepsilon_0$ denotes the initial yield stress and E is Young's modulus.

2.2. Finite plasticity

In elastic–plastic shells under a sufficiently high load, and in particular close to a crack tip, finite deformations generally occur, where the inelastic (plastic) part of the strains usually is large compared with the elastic part. The description of finite plastic deformations in conjunction with the Gurson model is often done by using the additive decomposition of the elastic and plastic strains rates (Tvergaard, 1989). In contrast to these works, we use the framework of multiplicative elastoplasticity which is widely accepted in this field. Its kinematic key assumption is the multiplicative split of the deformation gradient

$$\mathbf{F} = \mathbf{F}_{el}\mathbf{F}_{pl} \tag{6}$$

into an elastic and a plastic part, providing the basis of a geometrically exact theory and avoiding linearization of any measure of deformation. As a further advantage, fast and numerical stable algorithms,

proposed and described in Simo (1992), can be used. In the following, only a brief summary of the algorithm in the context of an FE implementation is given.

An essential aspect of Eq. (6) is the resulting additive structure of the actual logarithmic principal stretches within the return mapping scheme:

$$\boldsymbol{\epsilon}^{\mathrm{el}} = \boldsymbol{\epsilon}^{\mathrm{tr}} - \Delta\boldsymbol{\epsilon}^{\mathrm{pl}}. \tag{7}$$

Here, $\epsilon_i = \ln \lambda_i$ $(i = 1, 2, 3)$ and λ_i^2 are the eigenvalues of an elastic trial state, described by the left Cauchy–Green tensor $\mathbf{b}_{\mathrm{el}}^{\mathrm{tr}}$. The elastic strains $\boldsymbol{\epsilon}^{\mathrm{el}}$ are defined by Hooke's law and the plastic strain corrector $\Delta\boldsymbol{\epsilon}^{\mathrm{pl}}$ can be derived by the normality rule of plastic flow. The elastic left Cauchy–Green tensor can be specified with the decomposition (6) as

$$\mathbf{b}_{\mathrm{el}} = \mathbf{F}_{\mathrm{el}}\,\mathbf{F}_{\mathrm{el}}^{\mathrm{T}} = \mathbf{F}\,\mathbf{C}_{\mathrm{pl}}^{-1}\,\mathbf{F}^{\mathrm{T}}\,, \tag{8}$$

which clearly shows the "connection" between the elastic and plastic deformation measure by the occurrence of the plastic right Cauchy–Green tensor $\mathbf{C}_{\mathrm{pl}} = \mathbf{F}_{\mathrm{pl}}^{\mathrm{T}}\,\mathbf{F}_{\mathrm{pl}}$.

By means of the relative deformation gradient (Simo, 1992)

$$\mathbf{f} = \frac{\partial \mathbf{x}}{\partial \mathbf{x}_{n-1}} = \mathbf{F}\,\mathbf{F}_{n-1}^{-1}\,, \tag{9}$$

which relates the actual configuration $\mathbf{x}$ to the configuration belonging to the previous time step at t_{n-1}, an elastic trial-state is calculated for the current configuration at time t_n

$$\mathbf{b}_{\mathrm{el}}^{\mathrm{tr}} = \mathbf{f}\,\mathbf{b}_{n-1}\,\mathbf{f}^{\mathrm{T}} \tag{10}$$

with frozen internal variables at state t_{n-1}. If the condition $\Phi \leqslant 0$ is fulfilled by the actual stress state $\boldsymbol{\sigma}$, this state is possible and is so the actual stress state. If, on the other hand, $\Phi \leqslant 0$ is violated by the trial-state, in an additional step the trial stresses must be projected back on the yield surface $\Phi = 0$. This "return mapping" procedure is used as integration algorithm for the constitutive equations described in Section 2.1. It shall be mentioned that the algorithmic treatment in terms of principal axes has some advantages concerning computational aspects like time and memory saving. Based on this, the integration procedure of the constitutive equations for large and for small deformations (Aravas, 1987) is very similar.

3. Finite element formulation

3.1. 3D-element

The discretization chosen in this article is based on a standard 8-node-displacement element formulation with tri-linear shape functions N_i, $(i = 1, 2, \ldots, 8)$. Starting point is the weak form of equilibrium

$$g(\mathbf{u}, \delta\mathbf{u}) = \int_{\mathscr{B}} \boldsymbol{\sigma}\,\mathrm{grad}\,\delta\mathbf{u}\,\mathrm{d}v - \int_{\partial\mathscr{B}_\sigma} \mathbf{t}_L \cdot \delta\mathbf{u}\,\mathrm{d}a = 0 \tag{11}$$

formulated in the current configuration, where $\mathbf{u}$ is the displacement and $\mathbf{t}_L$ are the prescribed tractions acting on the boundary $\partial\mathscr{B}_\sigma$ of the body $\mathscr{B}$. Linearization with respect to the actual deformation state, and rearrangement leads with $\mathrm{d}v = J\,\mathrm{d}V$ after some steps to the following representation of the element stiffness:

$$Dg^{\mathrm{elmt}}(\hat{\mathbf{u}}, \delta\mathbf{u}) = \int_{\mathscr{B}_0} J\,(\Delta\boldsymbol{\sigma} + \mathrm{grad}\,\Delta\mathbf{u}\,\boldsymbol{\sigma})\mathrm{grad}\,\delta\mathbf{u}\,\mathrm{d}V^{\mathrm{elmt}}, \tag{12}$$

where $J = \det\mathbf{F}$ and $\mathscr{B}_0$ denotes the reference configuration. The load increment $\Delta\boldsymbol{\sigma}$ is calculated from the linearization of the 2. Piola–Kirchhoff tensor $\mathbf{S}$ as (Simo, 1992; Wriggers et al., 1996)

$$J\,\Delta\boldsymbol{\sigma} = \mathbf{F}\,\Delta\mathbf{S}\,\mathbf{F}^{\mathrm{T}}. \tag{13}$$

3.2. Underintegration and stabilization

The usual $2 \times 2 \times 2$-point-integration of the chosen element type shows an extreme "locking"-behaviour in shear-dominated problems. For this reason a 1-point-integration is used, which leads to a softer element behaviour. The terms omitted by this underintegration have to be taken into account by an artificial element stiffness stabilization matrix $\mathbf{K}_{\mathrm{stab}} = \mathbf{K}_{\mathrm{stab}}(\alpha_i, \gamma_i)$, where α_i is the artificial stiffness of the corresponding *eigen*mode γ_i, see Flanagan and Belytschko (1981). By this, the phenomenon known as hourglassing, which correlates to the eigenforms of the omitted terms, can be avoided, provided that values α_i in $\mathbf{K}_{\mathrm{stab}}$ are chosen in the magnitude of the shear modulus G.

The locking-free behaviour of this element formulation was successfully proved by solving the problem of the "pinched cylinder". This example is often used in the literature to test the efficiency of different element formulations for large deformations, see e.g. Wriggers et al. (1996). A comparison of the results based on the described 3D-element formulation with that of a shell element formulation (Wriggers et al., 1996) and that of a 3D-enhanced-strain element (Wriggers et al., 1996) show an excellent agreement in the load-displacement behaviour. Here, these results are omitted for the sake of brevity. As additional advantage of a reduced 1-point integration (which is important for 3D-models), the considerable reduction of computer memory used for storing the history variables on each integration point shall be mentioned. Compared with the $2 \times 2 \times 2$-point integration, the 1-point integration needs only $\frac{1}{8}$ of the history memory.

3.3. Solution procedure

To find a numerical solution for the nonlinear system of equations resulting from Eq. (11), a Newton–Raphson method is used. Within this global solution algorithm a solution $\Delta\mathbf{u}_n$ for the actual load step n has to be found from

$$\mathbf{K}\,\Delta\mathbf{u}_n = \mathbf{r}\,, \tag{14}$$

where $\mathbf{K}$ is the stiffness matrix. The standard treatment is a Gaussian elimination technique by a $\mathbf{LDL}^{\mathrm{T}}$-decomposition of $\mathbf{K}$ which is time and memory consuming. In contrast, in this study the iterative Lanczos procedure, Lanczos (1950) (with the modifications of Paige and Saunders (1975)) is used. It has the advantage of a remarkable reduction of the memory requirement by using a special storage technique Taylor (1985), making it highly favourable for large size 3D problems. For example, the memory required in the first example of Section 4 using a Gauss decomposition is 41 MByte while the Lanczos solver storing the stiffness matrix as *skyline* needs just 6.5 MByte. Regarding the CPU time, for the mentioned example both solvers need about the same time (60 s for one iteration step on an IBM RS/6000, working at about 20.7 Mflops). But with increasing problem size the Lanczos method is getting faster compared with the Gauss decomposition.

4. Examples and results

4.1. Test example: CT specimen

First, as a test example, crack initiation and growth in a CT specimen of German mild steel StE460 as shown in Fig. 1 is numerically simulated. For the same configuration and material, experimental and numerical results were reported in Klingbeil et al. (1993) and Klingbeil and Zadeh (1995). The material

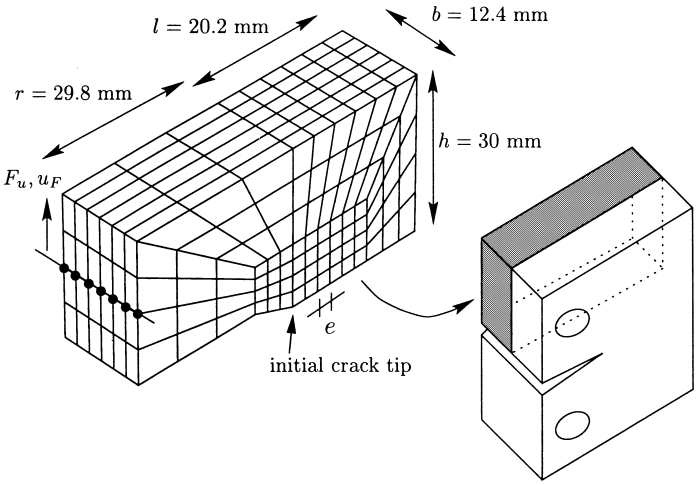

Fig. 1. CT Specimen and FE model.

parameter set (Table 1) is taken from Klingbeil et al. (1993) with only slight modifications in order to get a better approximation of the real matrix material behaviour in the transition region from the pure elastic to the pure plastic range (in Klingbeil et al. (1993) the parameters $\sigma_0 = 460\,\mathrm{MPa}$ and $N = 7$ were used). Since the two-parameter fit for the power law (5) from experimental data is dependent on the considered strain interval, these modifications may be tolerated. On account of the symmetry, only $\frac{1}{4}$ of the specimen has to be discretized.

As mentioned before, the FE results are mesh dependent on account of the strain softening character (loss of ellipticity) of the Gurson model. This problem might be overcome by regularizing the governing equations. As possible candidates e.g. nonlocal formulations, gradient formulations, Cosserat theories or viscoplastic material descriptions are discussed in the literature (Ehlers et al., 1998; Feucht et al., 1997). By all these formulations, an intrinsic "material length" is introduced. Because the physical basis of such a length is not yet clear in most of the cases, its introduction can be regarded as motivated more by the numerical argument of a regularization. Although, recent investigations (De Borst and Mühlhaus, 1992; Feucht et al., 1997) have shown that nonlocal and gradient formulations may lead to mesh-independent results, these methods are not used here on account of their numerical expense. As a simple alternative, a "quasi-material" length is introduced which is defined by the edge length of the finite elements in the damaging region ahead and around the crack tip. This procedure, which was also successfully used in other investigations (Hutchinson, 1997; Klingbeil et al., 1993; Klingbeil and Zadeh, 1995), consists in the numerical simulation of a fracture test with fixed material data by only varying the finite element edge length. The "correct" length is determined by matching the crack initiation loads from the experiment and from the simulations. This length is then regarded like a material parameter which cannot be changed for simulations of other test specimen or structures made from the same material.

By applying this procedure to the CT specimen and using the experimental data from Klingbeil and Zadeh (1995) (with an initiation load $F_\mathrm{u} \simeq 22.3$ kN), the finite element edge length finally was set to

Table 1
Material parameters

E (MPa)	ν	σ_0 (MPa)	N	q_1	f_0	f_c	f_f	f_N	ε_N	s_N
210000	0.3	450	5	1.5	0.0025	0.021	0.19	0.01	0.3	0.1

$l_e = 0.2$ mm. Here, crack initiation was defined by the first failure of an element (at f_f), and its switch-off by a specific "node-skipping-technique". In Fig. 2, the load–displacement curves from the experiment (taken from Klingbeil and Zadeh (1995)) and from our numerical simulation with $l_e = 0.2$ mm are compared. Both curves are in good agreement. The slight difference of the crack initiation point may be explained by an unprecise l_e and the uncertainties of the exact determination of the crack initiation instant in the simulation as well as in the experiment. The typical damage distribution on the ligament at the instant of crack initiation is depicted in Fig. 3. It can be seen that the damage is concentrated directly in front of the initial crack tip with increasing f towards the middle region of the specimen. This behaviour was also found in the investigations of Shih et al. (1997) and Klingbeil and Zadeh (1995). Because at crack initiation, the first elements have been already switched-off, the highest f-values appear at a short distance ahead of the initial crack front.

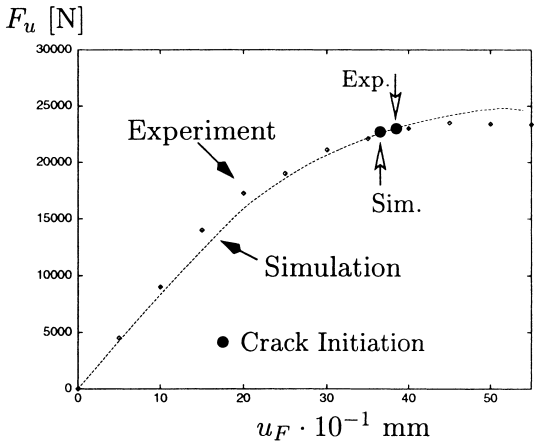

Fig. 2. Load–displacement curve: experiment and simulation.

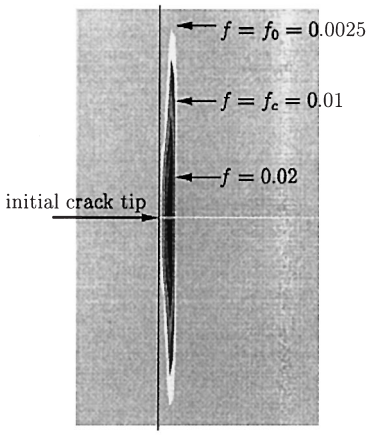

Fig. 3. Damage distribution in the ligament at crack initiation.

4.2. Cylindrical shell containing a crack

The capability of the used model is demonstrated in the following with the example of a through-cracked cylindrical shell of moderate thickness under a pressure load p. First, a shell containing an axial crack as shown in Fig. 4 with the geometry parameters of Table 2 is considered. The finite element discretization in the region, indicated in Fig. 4, is realized by a mesh generator Rank et al. (1992) for a 2D-wind-off and then expanded in the thickness direction by moving the nodal coordinates. In this example, the wall thickness consists of three element layers. Therefore, the model is able to capture the shell-bending effects and (at least roughly) the damage distribution across the wall thickness. Since the material is assumed to be the same as in the test example, the mesh size ahead and around the crack tip is set to $l_e = 0.2$ mm. The realized mesh, consisting of 2464 nodes defining 1629 brick elements, is depicted in Figs. 4 and 6. The chosen boundary conditions represent a periodic continuation of the structure in axial and circumferential direction. The pressure p is applied by attaching it to nodal force values depending on the actual configuration (Schweizerhof and Ramm, 1984) at the inner surface nodes of the shell. Because a pressure load controlled simulation is impossible in the crack initiation and softening load regime, an arc-length procedure is used to control the load (belonging to an actual load step) and to find the stable solution branch.

The global behaviour of the structure is represented by the "pressure vs. load steps"-diagram in Fig. 5, in which crack initiation and growth is indicated additionally. With increasing load steps the pressure first rises up to a peak load and then decreases continuously. Conspicuous is the instant of crack initiation at a load level of 80 ($p = 0.82$ MPa), appearing distinctly behind the pressure maximum at load level 60 ($p = 0.84$ MPa). This global softening of the structure before crack initiation might be explained by the

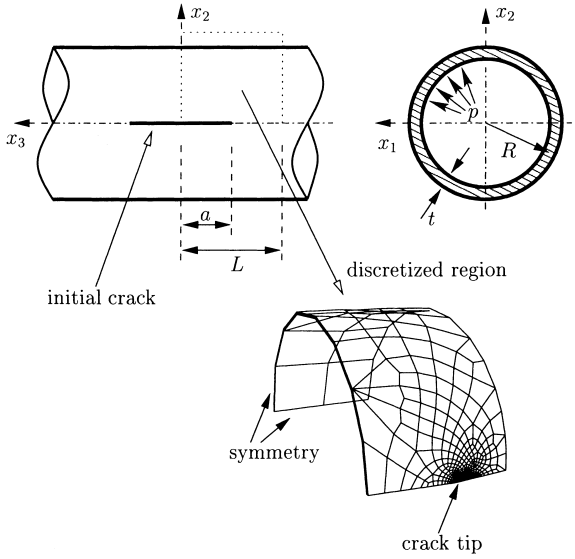

Fig. 4. Shell with axial crack.

Table 2
Geometry data: shell containing an axial crack

L (mm)	R (mm)	t (mm)	a (mm)	l_e (mm)
50.0	50.0	1.0	30.0	0.2

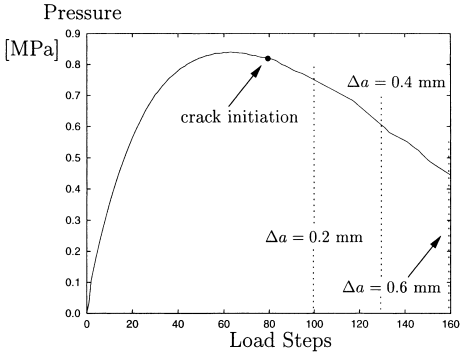

Fig. 5. Pressure vs. load steps.

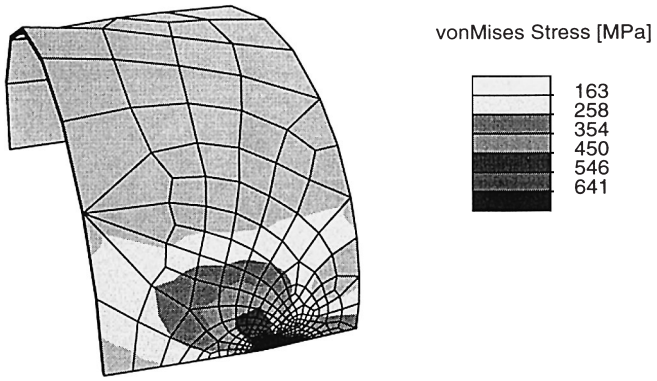

Fig. 6. von Mises stress – axial crack.

finite (outward directed) deformations of the crack face regions, resulting in additional strains through bending. In this context it should be mentioned that the pressure p always acts perpendicular to the deformed shell surface. Further crack advance after initiation occurs in the softening regime at higher load steps. It is self-evident that such a behaviour is only possible under strain controlled (deformation controlled) loading. Under pressure controlled circumstances (and taking not into account crack initiation), the peak load would characterize an instability point of the structure. When allowing crack initiation, a snap-through phenomenon at crack initiation pressure would occur, accompanied by an unstable crack growth. It should be emphasized that the computational catch-up of the global softening behaviour is just possible by the used arc-length method, allowing to find a stable global solution despite the decreasing pressure.

In Fig. 6, the von Mises equivalent stress distribution in the outer shell surface at crack initiation (load step 80) is shown for the discretized region. It is remarkable that the plastic zone size, characterized by the initial flow stress $\sigma_0 = 450\,\mathrm{MPa}$, is relatively small. This behaviour is qualitatively comparable with that of a CCT specimen. The details of the damage and stress distribution in the near-tip region at different load levels are illustrated in Fig. 7. Shown are f and σ_{eqv} across the wall thickness and the outer shell surface as well as the crack front advance Δa at load level 100, 130 and 160. As already mentioned, crack initiation occurs at a load level of 80, which is numerically indicated by the failure and switch-off of the first element – here the middle element ahead of the initial crack front. At a load level of 100, the failure of two elements (that in the middle and that at the inner surface) is visible. At a load level of 130, the crack front has

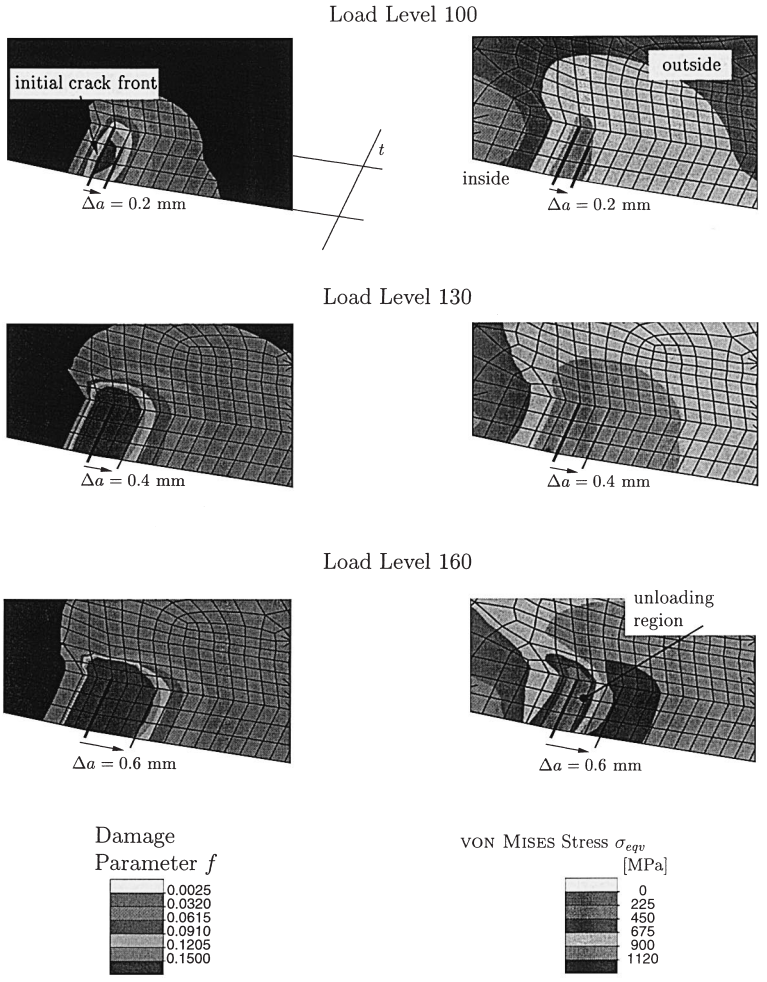

Fig. 7. Zoom out – axial crack.

propagated by two elements across the whole wall thickness and finally a $\Delta a = 0.6$ mm can be observed at load level 160. As the crack growths the fields of f and σ_{eqv} are varying. Further it can be seen that the high level region of both fields is shifted slightly from the middle surface towards the inner surface of the shell at all load levels. At a load level of 160, an unloading region between the initial and the actual crack front has developed.

Next, a shell of the same geometry and loading, containing a circumferential crack as represented in Fig. 8 and with the geometry parameters of Table 3, is considered. Only a few results shall be discussed for this case. Fig. 9 shows the distribution of the equivalent stress at load step 90 ($p = 0.12$ MPa), which in essential parts differs from that for the axial crack. While the load step 90 characterizes in the case of an axial crack a deformation state after crack initiation, no crack advance has appeared this instant for the circumferential crack. In the present case, the stress gradients normal to the ligament are not as high as for the axial crack. As a consequence, the plastic zone and deformation is not as localized as for the axial crack. Further, the shift of the stress concentration across the wall towards the inner shell surface is now significantly more pronounced as for the axial crack. In addition to these results, the deformation of the mesh (enlarged 20

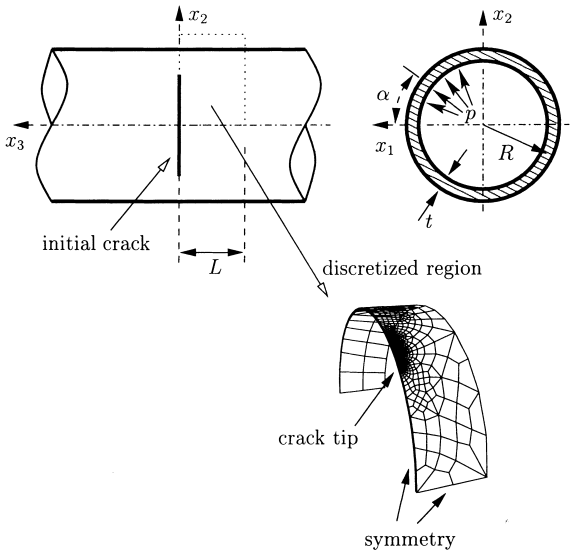

Fig. 8. Shell with circumferential crack.

Table 3
Geometry data: shell containing a circumferential crack

L (mm)	R (mm)	t (mm)	α (°)	l_e (mm)
25.0	50.0	1.0	45.0	0.2

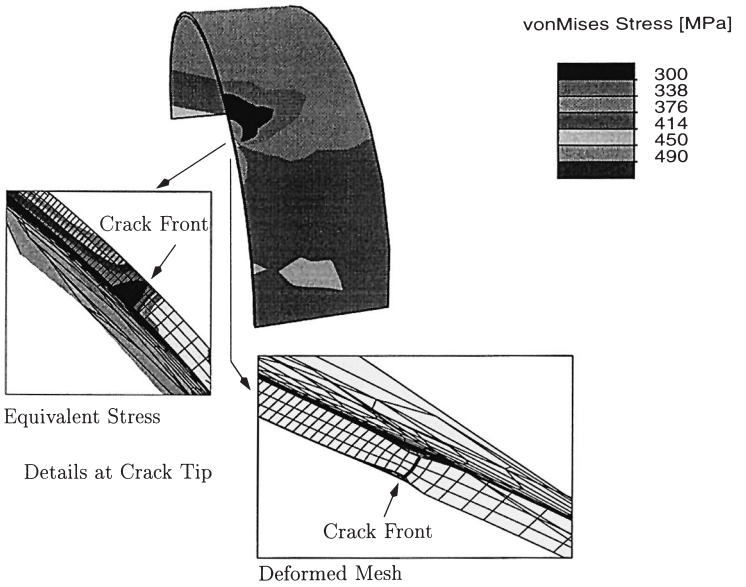

Fig. 9. Results at load step 90 – circumferential crack.

times for a better representation) around the crack tip is shown in Fig. 9. From this figure the wall necking of the wall at the crack front clearly can be seen.

It shall be emphasized that the global loading of the circumferential crack differs essentially from the axial crack since no resultant axial load results from the internal pressure. Keeping this in mind, the different local behaviour around the crack front may be expected.

References

Aravas, N., 1987. On the numerical integration of a class of pressure-dependent plasticity models. International Journal for Numerical Methods in Engineering 24, 1395–1416.

Baaser, H., Gross, D., 1998a. Damage and strain localisation during crack propagation in thin-walled shells. In: Bertram, A., Sidoroff, F. (Eds.), Mechanics of Materials with Intrinsic Length Scale. EDP Sciences, Magdeburg, Germany, pp. 13–17, Journal de Physique IV, 8.

De Borst, R., Mühlhaus, H.-B., 1992. Gradient-dependent plasticity: Formulation and algorithmic aspects. International Journal for Numerical Methods in Engineering 35, 521–539.

Ehlers, W., Diebels, S., Volk, W., 1998. Deformation and compatibility for elasto–plastic micropolar materials with applications to geomechanical problems. In: Bertram, A., Forest, S., Sidoroff, F. (Eds.), Mechanics of Materials with Intrinsic Length Scale. Magdeburg, Germany, pp. 120–127.

Feucht, M., Gross, D., Wriggers, P., 1997. A new element formulation for nonlocal damage models. In: Owen, D.R.J., Onate, E., Hinton, E. (Eds.), Computational Plasticity. Barcelona, Spain, pp. 1083–1088.

Flanagan, D.P., Belytschko, T., 1981. A uniform strain hexahedron and quadrilateral with orthogonal hourglass control. International Journal for Numerical Methods in Engineering 17, 679–706.

Gurson, A.L., 1977. Continuum theory of ductile rupture by void nucleation and growth: Part I – yield criteria and flow rules for porous ductile media. Journal of Engineering Materials and Technology 99, 2–15.

Hutchinson, J.W., 1997. Linking scales in fracture mechanics. In: Karihaloo, B.L., Mai, Y.-W., Ripley, M.I., Ritchie, R.O. (Eds.), Advances in Fracture Research. Vol. 1. Sydney, Australia, pp. 1–14.

Klingbeil, D., Künecke, G., Schicker, J., 1993. On the application of Gurson's model to various fracture mechanics specimens. Report 1.31 93/3. BAM. Berlin.

Klingbeil, D., Zadeh, Moussavi, G., 1995. On the simulation of ductile crack growth in fracture mechanics specimens using the Gurson model. In 'SMiRT 13'. Porto Alegre, Brazil. SMiRT 13.

Lanczos, C., 1950. An iteration method for the solution of eigenvalue problems of linear differential and integral operators. Journal of Research of the National Bureau of Standards 45, 409–436.

Paige, C.C., Saunders, M.A., 1975. Solution of sparse indefinite systems of linear equations. SIAM Journal of Numerical Analysis 12, 617–629.

Rank, E., Schweingruber, M., Sommer, M., 1992. Adaptive mesh generation and transformation of triangular to quadrilateral meshes. Communications in Applied Numerical Methods 9, 121–129.

Roehl, D., Ramm, E., 1996. Large elasto–plastic finite element analysis of solids and shells with the enhanced assumed strain concept. International Journal of Solids and Structures 33, 3215–3237.

Schweizerhof, K., Ramm, E., 1984. Displacement dependent pressure loads in nonlinear finite element analyses. Computers and structures 18, 1099–1114.

Shih, C.F., Cheng, L., Faleskog, J., Gao, X., 1997. A cell model for ductile fracture with applications to the transition regime. In: Karihaloo, B.L., Mai, Y.-W., Ripley, M.I., Ritchie, R.O. (Eds.), Advances in Fracture Research. vol. 4. Sydney, Australia, pp. 1935–1946.

Simo, J.C., 1992. Algorithms for static and dynamic multiplicative plasticity that preserve the classical return mapping schemes of the infinitesimal theory. Computer Methods in Applied Mechanics and Engineering 99, 61–112.

Taylor, R.L., 1985. Solution of linear equations by a profile solver. Engineering Computations 2, 344–350.

Tvergaard, V., 1989. Material failure by void growth to coalescence. Advances in Applied Mechanics 27, 83–151.

Wriggers, P., Eberlein, R., Reese, S., 1996. A comparison of three-dimensional continuum and shell elements for finite plasticity. International Journal of Solids and Structures 33, 3309–3326.